Supplementary Information: Emergent probability fluxes in confined microbial navigation

Jan Cammann,[1,2,*] Fabian Jan Schwarzendahl,[3,4,2,*] Tanya Ostapenko,[2] Danylo Lavrentovich,[2] Oliver Bäumchen,[2,5] and Marco G. Mazza[1,2]

[1] *Interdisciplinary Centre for Mathematical Modelling and Department of Mathematical Sciences, Loughborough University, Loughborough, Leicestershire LE11 3TU, United Kingdom*
[2] *Max Planck Institute for Dynamics and Self-Organization, Am Faßberg 17, 37077 Göttingen, Germany*
[3] *Institut für Theoretische Physik II: Weiche Materie, Heinrich-Heine-Universität Düsseldorf, 40225 Düsseldorf, Germany*
[4] *Department of Physics, University of California, Merced, 5200 N. Lake Road, Merced, California 95343, USA*
[5] *Experimental Physics V, University of Bayreuth, Universitätsstr. 30, 95447 Bayreuth, Germany*

I. NUMERICAL COMPUTATION OF NONEQUILIBRIUM FLUXES

We numerically compute the nonequilibrium probability fluxes using a method introduced by Battle et al. [1]. We divide positional space into equally sized square boxes (i, j) of side Δx, where i and j denote the box's position in x_1 and x_2 direction. From the recorded trajectories of the *Chlamydomonas* cells we construct a time series $A(t_n)$ containing information about the cell's location $(i, j)_n$ (the box it resides in) at time t_n, and the time $t_{n,n+1}$ spent in the state $(i, j)_n$ before the transition to the new state $(i, j)_{n+1}$ occurs. Quite generally, $A(t_n)$ in matrix form reads

$$A(t_n) = \begin{bmatrix} (i,j)_1 & (i,j)_2 & t_{1,2} \\ (i,j)_2 & (i,j)_3 & t_{2,3} \\ & \vdots & \\ (i,j)_{N-1} & (i,j)_N & t_{N-1,N} \end{bmatrix}, \tag{S1}$$

where the index n indicates the discrete time steps, and N is the total length of the time series. Limited time resolution of the continuous trajectory $\boldsymbol{x}(t) \to (i, j)_n$ might lead to entries in A where two successive states $(i, j)_n$ and $(i, j)_{n+1}$ do not correspond to adjacent boxes. In such cases, we determine the intermediate boxes via linear interpolation and insert them into $A(t_n)$, such that contiguous rows in $A(t_n)$ correspond to neighboring boxes.

The stochasticity of the system necessitates a large amount of statistics to identify significant fluxes. To maximize the amount of available data, the trajectories recorded experimentally were mirrored along the symmetry axes of the elliptical compartments, effectively quadrupling the amount of available trajectory data. The transition rates $w_{(i,j),(k,l)}$ between boxes (i, j) and (k, l) can be calculated by counting all rows of $A(t_n)$ containing a transition from (i, j) to (k, l) and those that contain transitions in the opposite direction

$$w_{(i,j),(k,l)} = \frac{1}{t_{\text{total}}} \Big(N_{(i,j),(k,l)} - N_{(k,l),(i,j)} \Big), \tag{S2}$$

where $N_{(i,j),(k,l)}$ denotes the number of transitions from box (i, j) to (k, l), $N_{(k,l),(i,j)}$ the number of transitions in the opposite direction, and t_{total} the total duration of the trajectory. The coarse-grained probability flux corresponding to box (i, j) is then calculated as

$$\boldsymbol{j}_{(i,j)} = \frac{1}{2\Delta x} \begin{pmatrix} w_{(i-1,j)(i,j)} + w_{(i,j)(i+1,j)} \\ w_{(i,j-1)(i,j)} + w_{(i,j)(i,j+1)} \end{pmatrix}. \tag{S3}$$

By bootstrapping the rows of $A(t_n)$ we can calculate statistical uncertainties of the coarse-grained flux $\boldsymbol{j}$, and by probing for correlations between consecutive rows one gains information about whether the system is Markovian or not. For more details on such procedures the reader may be referred to the supplemental material of [1].

---

* equal contribution

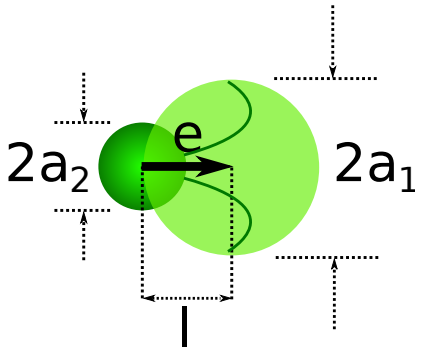

FIG. S1. In simulations the swimmer is modelled as an asymmetric dumbbell of two spheres a distance l apart. The back sphere represents the cell body and the front sphere models the stroke averaged shape of the flagella, which are beating fast enough, that on the relevant time scales for steric interactions they can be approximated as a solid sphere.

To ensure sufficient resolution of the experimental fluxes the long axis of the ellipse is divided into 50 bins. For the simulations, 80 bins along the long ellipse axis were used. Non-elliptical compartments were resolved at a similar scale. Using circular compartments (where fluxes are absent), we estimate the background noise due to the finiteness of statistics to be $\mathcal{F}_{\text{noise}} \approx (5 \pm 0.6) \times 10^{-3}$ shown by a gray horizontal line in Fig. 4.

II. ANALYTICAL TREATMENT

From the microscopic Eqs. (5-7) we compute the Fokker–Planck equation for the probability $p = p(\boldsymbol{r}, \boldsymbol{e}, t)$ to find a *C. reinhardtii* cell, which reads

$$\frac{\partial p}{\partial t} = -\boldsymbol{\nabla} \cdot \Big(v_0 \boldsymbol{e} + \mu_w \boldsymbol{F_w} - D_T \boldsymbol{\nabla}\Big) p - \boldsymbol{e} \times \frac{\partial}{\partial \boldsymbol{e}} \cdot \left(\frac{1}{\tau_w} \boldsymbol{e} \times \boldsymbol{G}_w - D_R \boldsymbol{e} \times \frac{\partial}{\partial \boldsymbol{e}}\right) p. \tag{S4}$$

Here we used the approximation that both force $\boldsymbol{F}_w = \boldsymbol{F}_w(\boldsymbol{r})$ and gorque G_w, $\boldsymbol{T}_w = \boldsymbol{e} \times \boldsymbol{G}_w(\boldsymbol{r})$, only depend on the position $\boldsymbol{r}$. Equation S4 can be written symbolically as

$$\frac{\partial p}{\partial t} = -\boldsymbol{\mathcal{L}} \cdot \boldsymbol{\mathcal{J}} \tag{S5}$$

with the following definitions

$$\boldsymbol{\mathcal{L}} = \begin{pmatrix} \boldsymbol{\nabla} \\ \boldsymbol{e} \times \frac{\partial}{\partial \boldsymbol{e}} \end{pmatrix}, \tag{S6}$$

$$\boldsymbol{\mathcal{J}} = \begin{pmatrix} v_0 \boldsymbol{e} + \mu_w \boldsymbol{F}_w - D_T \boldsymbol{\nabla} \\ \frac{1}{\tau_w} \boldsymbol{e} \times \boldsymbol{G}_w - D_R \boldsymbol{e} \times \frac{\partial}{\partial \boldsymbol{e}} \end{pmatrix} p\,, \tag{S7}$$

for the operator $\mathcal{L}$ and probability flux $\mathcal{J}$.

To make progress with Eq. (S4) we use a multipole expansion and compute equations for the density $\rho(\boldsymbol{r}) = \int p(\boldsymbol{r}, \boldsymbol{e}, t) \mathrm{d}\boldsymbol{e}$ and polarization $\boldsymbol{P}(\boldsymbol{r}) = \int \boldsymbol{e} p(\boldsymbol{r}, \boldsymbol{e}, t) \mathrm{d}\boldsymbol{e}$, which read

$$\frac{\partial \rho}{\partial t} = -\boldsymbol{\nabla} \cdot (v_0 \boldsymbol{P} + \mu_w \boldsymbol{F}_w \rho - D_T \boldsymbol{\nabla} \rho) + \boldsymbol{P} \cdot \boldsymbol{G}_w, \tag{S8}$$

$$\frac{\partial \boldsymbol{P}}{\partial t} = -\frac{1}{2} \left(v_0 \boldsymbol{\nabla} - \frac{1}{\tau_w} \boldsymbol{G}_w\right) \rho - \mu_w \boldsymbol{\nabla} \cdot (\boldsymbol{F}_w \boldsymbol{P}) + D_T \boldsymbol{\nabla}^2 \boldsymbol{P} - D_R \boldsymbol{P}. \tag{S9}$$

To find the nonequilibrium flux of the density ρ, we now compute the orientational average of the probability flux Eq.(S7), which can be expressed in terms of the density and polarization

$$\int \boldsymbol{\mathcal{J}} \mathrm{d}^2 \boldsymbol{e} = \begin{pmatrix} v_0 \boldsymbol{P} + \mu_w \boldsymbol{F}_w \rho - D_T \boldsymbol{\nabla} \rho \\ \frac{1}{\tau_w} \boldsymbol{P} \times \boldsymbol{G}_w \end{pmatrix} = \begin{pmatrix} \boldsymbol{j}_r \\ \boldsymbol{j}_e \end{pmatrix}, \tag{S10}$$

which defines the translational flux $\boldsymbol{j}_r$ and rotational flux $\boldsymbol{j}_e$. The translational flux can be identified in Eq.(S8), which then simplifies to

$$\frac{\partial \rho}{\partial t} = -\boldsymbol{\nabla} \cdot \boldsymbol{j}_r + \boldsymbol{P} \cdot \boldsymbol{G}_w. \tag{S11}$$

If we now assume a nonequilibrium steady state we arrive at

$$\boldsymbol{\nabla} \cdot \boldsymbol{j}_r = \boldsymbol{P} \cdot \boldsymbol{G}_w. \tag{S12}$$

Here, it is worth pointing out that $\boldsymbol{G}_w$ is only nonzero at the boundary. Since the *C. reinhardtii* cell swims mostly parallel to the wall, $\boldsymbol{P}$ is parallel to the wall; further, $\boldsymbol{G}_w$ is by definition normal to the wall; thus it follows

$$\boldsymbol{\nabla} \cdot \boldsymbol{j}_r = 0. \tag{S13}$$

This condition states that the nonequilibrium fluxes are divergence-free. To determine the nonequilibrium fluxes we now use the vector-potential definition of stream function $\boldsymbol{j}_r = \nabla \times \boldsymbol{\psi}$, where the vector potential $\boldsymbol{\psi} \equiv \begin{pmatrix} 0 \\ 0 \\ \psi \end{pmatrix}$, that is, in coordinates

$$\begin{pmatrix} j_{r,x} \\ j_{r,y} \\ 0 \end{pmatrix} = \nabla \times \begin{pmatrix} 0 \\ 0 \\ \psi \end{pmatrix}. \tag{S14}$$

We can find a governing equation for $\boldsymbol{\psi}$ by considering the vorticity $\omega = \partial_x j_{r,y} - \partial_y j_{r,x}$ and using Eq. (S14). This leads to a divergence-free $\boldsymbol{j}_r$ that is determined by the following Poisson equation

$$\Delta \psi = -\omega\,. \tag{S15}$$

The vorticity can be determined using the definition of the nonequilibrium flux in Eq. (S10)

$$\begin{pmatrix} 0 \\ 0 \\ \omega \end{pmatrix} = \nabla \times \begin{pmatrix} j_{r,x} \\ j_{r,y} \\ 0 \end{pmatrix} = \nabla \times \boldsymbol{j}_r = \nabla \times (v_0 \boldsymbol{P} + \mu_w \boldsymbol{F_w} \rho - D_T \boldsymbol{\nabla} \rho). \tag{S16}$$

The last term on the right-hand side of Eq. (S16) vanishes identically; the second term can be rewritten as

$$\mu_w \nabla \times \boldsymbol{F_w} \rho = \mu_w (\rho \nabla \times \boldsymbol{F_w} + \nabla \rho \times \boldsymbol{F_w})\,, \tag{S17}$$

where the first term vanishes since $\boldsymbol{F_w}$ is the gradient of a potential. After these simplifications, the vorticity reads

$$\begin{pmatrix} 0 \\ 0 \\ \omega \end{pmatrix} = v_0 \nabla \times \boldsymbol{P} + \mu_w \nabla \rho \times \boldsymbol{F_w}. \tag{S18}$$

We now derive an expression for the curl of the polarization, $\nabla \times \boldsymbol{P}$. In the steady state, the polarization equation reads (see Eq. (S9))

$$0 = -\frac{1}{2}\left(v_0 \boldsymbol{\nabla} - \frac{1}{\tau_w} \boldsymbol{G}_w\right) \rho - \mu_w \boldsymbol{\nabla} \cdot (\boldsymbol{F}_w \boldsymbol{P}) + D_T \boldsymbol{\nabla}^2 \boldsymbol{P} - D_R \boldsymbol{P}\,. \tag{S19}$$

Taking the curl of Eq.(S19), and neglecting translational diffusion gives

$$0 = \frac{1}{2\tau_w} \nabla \times (\boldsymbol{G}_w \rho) - \mu_w \boldsymbol{\nabla} \times (\boldsymbol{P} \nabla \cdot \boldsymbol{F}_w + \boldsymbol{F}_w \nabla \cdot \boldsymbol{P}) - D_R \nabla \times \boldsymbol{P}. \tag{S20}$$

Since the *C. reinhardtii* cell swims mostly parallel to the wall, we do not expect a large divergence of the polarization close to the boundary and thus we can neglect the term $\boldsymbol{F}_w \nabla \cdot \boldsymbol{P}$ in Eq. (S20); additionally, the term $\nabla(\nabla \cdot \boldsymbol{F}_w)$ is approximately parallel to the wall, and hence to $\boldsymbol{P}$. The curl of the polarization reads

$$\nabla \times \boldsymbol{P} = \frac{\nabla \times (\boldsymbol{G}_w \rho)}{2\tau_w (\mu_w \boldsymbol{\nabla} \cdot \boldsymbol{F}_w + D_R)}\,. \tag{S21}$$

Plugging Eq. (S21) into Eq. (S18) gives

$$\begin{pmatrix}0\\0\\\omega\end{pmatrix} = v_0 \frac{\nabla \times (\boldsymbol{G}_w \rho)}{2\tau_w(\mu_w \boldsymbol{\nabla}\cdot \boldsymbol{F}_w + D_R)} + \mu_w \nabla\rho \times \boldsymbol{F_w}. \tag{S22}$$

Here, it is worth noting that all terms that lead to a vorticity in Eq. (S22) act only at the boundary of the compartment. From [2] we know that the density at the wall approximately scales with the curvature $\rho_{\text{wall}} \approx \alpha\kappa$, where κ is the local curvature at the wall and α is a constant. Furthermore, the gorque $\boldsymbol{G}_w$ is a gradient of a potential such that Eq. (S22) can be simplified to

$$\omega = v_0\alpha \frac{G_{w,y}\partial_x\kappa - G_{w,x}\partial_y\kappa}{2\tau_w(\mu_w \boldsymbol{\nabla}\cdot \boldsymbol{F}_w + D_R)} + \mu_w(F_{w,y}\partial_x\kappa - F_{w,x}\partial_y\kappa). \tag{S23}$$

Using Eq. (S23) for the vorticity in Eq. (S15) gives

$$\Delta\psi = -v_0\alpha \frac{G_{w,y}\partial_x\kappa - G_{w,x}\partial_y\kappa}{2\tau_w(\mu_w \boldsymbol{\nabla}\cdot \boldsymbol{F}_w + D_R)} - \mu_w(F_{w,y}\partial_x\kappa - F_{w,x}\partial_y\kappa), \tag{S24}$$

which can be solved exactly (see next Section).

III. SOLUTION OF POISSON EQUATION

The Green's function of the two-dimensional Poisson equation in an ellipse is given by[3]

$$G(z,z_0) = -\frac{1}{2\pi}\ln\frac{2|z-z_0|}{A+B} + \frac{1}{2\pi}\sum_{k=0}^{\infty}\ln\left|\frac{4q^{4k+1}[z^2+(z_0^*)^2] - 4q^{2k}(1+q^{4k+2})zz_0^* + (A+B)^2(1-q^{4k+2})^2}{4q^{4k+3}(z^2+z_0^2) - 4q^{2k+1}(1+q^{4k+4})zz_0 + (A+B)^2(1-q^{4k+4})^2}\right|, \tag{S25}$$

where we use the complex variables $z = x + iy$ for the position and $z_0 = x_0 + iy_0$ for the position of the source at (x_0, y_0), A and B are the semi-major and semi-minor axes of the ellipse, respectively, and $q = (A-B)/(A+B)$.

Formally the solution of the Poisson equation (S15) is then given by the convolution (denoted with $*$) of Eq. (S23) and Eq. (S25), which reads

$$\psi = G * \omega\,. \tag{S26}$$

We approximate the convolution by placing "point charges" close to the boundary in the region $\mathcal{B}$ where the force (and gorque) acts

$$\psi \approx \sum_{z_0\in\mathcal{B}} G(z,z_0)\omega(z_0), \tag{S27}$$

where we use Eq. (S23) for computing $\omega(z_0)$. Note that since $\omega(z)$ is only nonzero at the boundary, it is sufficient to evaluate Eq. (S27) at the boundary.

To explicitly compute Eq. (S27), we define a small boundary region $\mathcal{B}$, which corresponds to the region in which forces act on our dumbbell swimmer (see also Methods section of the main text). Explicitly, the boundary region $\mathcal{B}$ is defined by an inner ellipse $\mathcal{E}_{\text{start}}$ and an outer ellipse $\mathcal{E}_{\text{stop}}$. Here, $\mathcal{E}_{\text{start}}$ is characterized by the major half axis $A - a_2$ and minor half axis $B - a_2$, where a_2 is the size of the small circle of the dumbbell. $\mathcal{E}_{\text{stop}}$ is characterized by the major half axis $A - (2^{1/6}a_1)$ and minor half axis $B - (2^{1/6}a_1)$, where a_1 is the size of the large circle of the dumbbell and the factor $2^{1/6}$ stems from the range of the Weeks–Chandler–Anderson potential used to evaluate the forces.

To numerically evaluate Eq. (S27) we further approximate the source term $\omega(z_0)$. Given a curvature κ at the wall we numerically compute the source term $\omega(z_0)$ for a range of distances from the wall and average them to obtain $\omega_{\text{avr}}(\kappa)$. To find the source term $\omega(z_0)$ at a $z_0 \in \mathcal{B}$ we then compute the local κ curvature and find a corresponding $\omega_{\text{avr}}(\kappa)$, which is then used to evaluate Eq. (S27). We have to use this procedure since a simple evaluation of $\omega(z_0)$ strongly fluctuates and depends on the number of discretization points. Thus a simple evaluation of the sum Eq. (S27) does not give physical results. Using our averaging procedure, however, we obtain a smooth approximation of $\omega(z_0)$ that does not fluctuate nor depend on the number of discretization points.

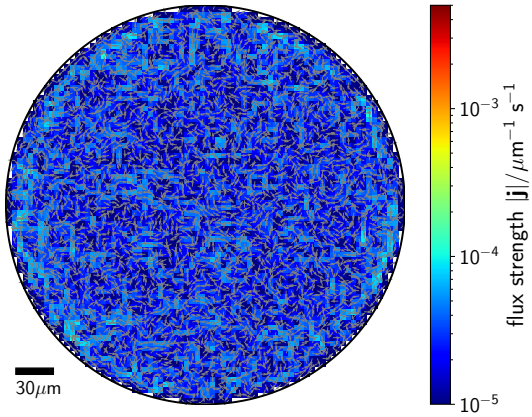

FIG. S2. Nonequilibrium fluxes inside a circular chamber, obtained from Brownian dynamics simulations of an asymmetric dumbbell. No directed fluxes are observed.

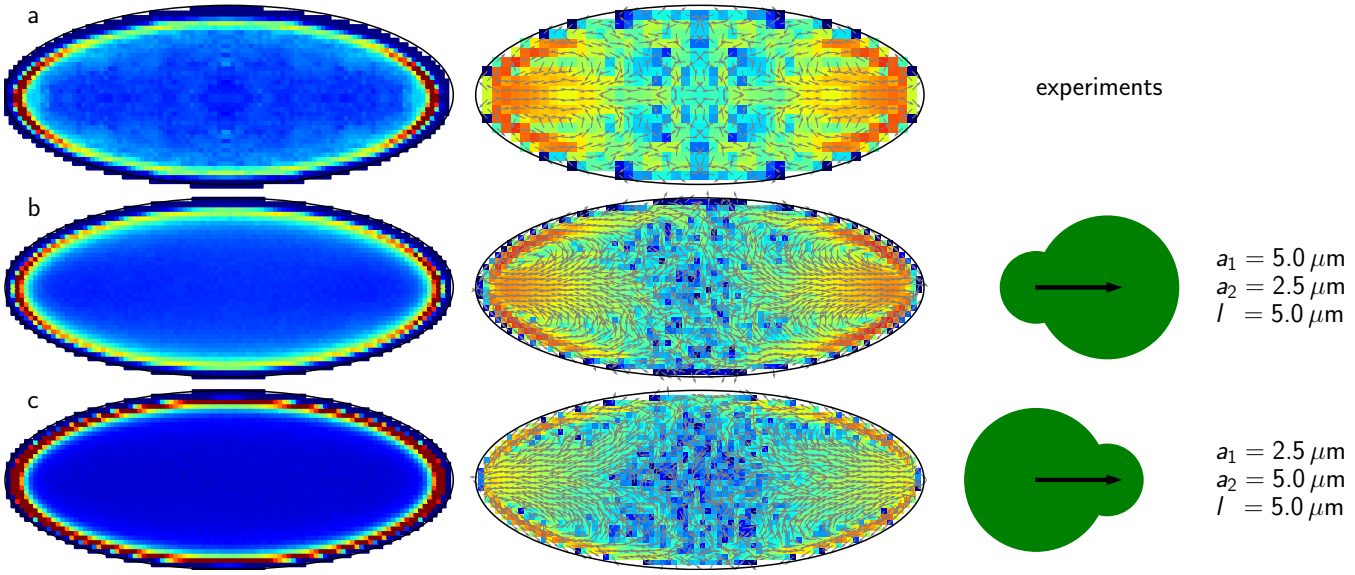

FIG. S3. Comparison of relative probability density (left) and probability fluxes (right) as measured in (a) experiments, (b) from simulations of a swimmer with the fore-aft asymmetry of *Chlamydomonas* (see also Methods), and (c) inverted asymmetry. Results in (b) reproduce the experimental observations most accurately.

IV. NONEQUILIBRIUM FLUX IN CIRCULAR COMPARTMENT

Figure S2 shows the nonequilibrium fluxes computed from Brownian dynamics simulations of an asymmetric dumbbell (see Eqs. 5-7) inside a circular compartment. We do not find any directed fluxes inside the circular chamber. This results from the fact that the underlying equations of motion are symmetric in the polar angle (The effect of activity and the corresponding nonequilibrium fluxes in circular chambers can be observed by considering the phase space spanned the radial position and the orientation of the active particle.). However, in elliptical chambers the equations of motion are not symmetric in the polar angle.

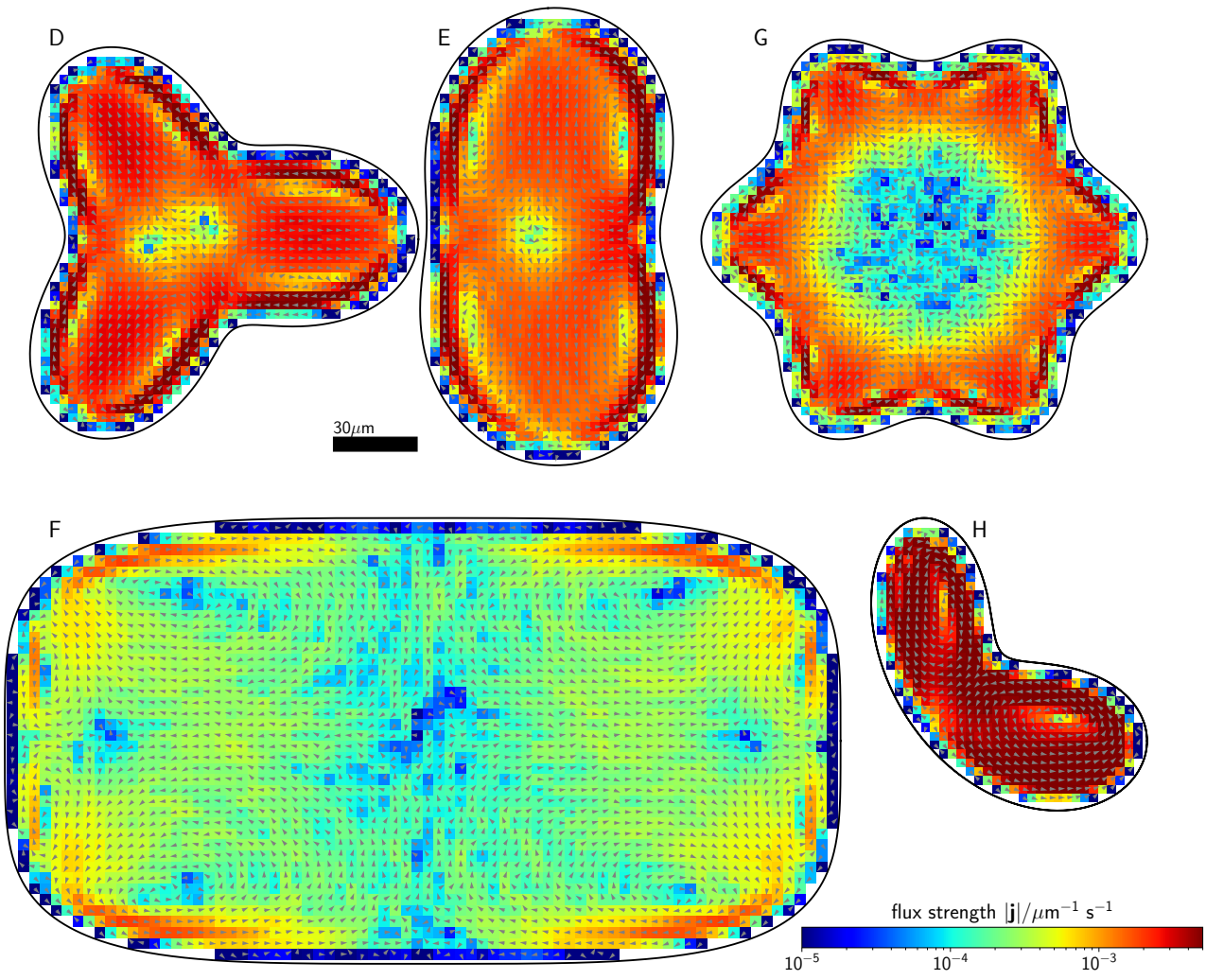

FIG. S4. Complexity and topology of flux loops. Complex geometric confinement confirms the topological features of the flux loops. The nonequilibrium fluxes are extracted from our active Brownian dynamics simulations. Fluxes are dominated by gradients of wall curvature. The mathematical formulas of the shown compartments are provided in SI Sec. VI.

V. ALTERNATE SWIMMER GEOMETRIES

The emergence of probability fluxes is a direct consequence of active motion and confinement. The choice of geometry of the swimming cell will not qualitatively alter our results, but has quantitative consequences. When direct comparison with experiments is considered, our model (see Methods and Fig. S1) reproduces the experimental probability fluxes and relative probability density most accurately. As an example, the probability fluxes calculated from experiments and simulations of a swimmer with the fore-aft asymmetry of *Chlamydomonas* and the reversed one are compared in Fig. S3.

VI. OTHER COMPARTMENT GEOMETRIES AND FURTHER COMPARISONS WITH EXPERIMENTS

The simulation results shown in Fig. 3 and Fig. S4 where obtained by simulating the dynamics of the introduced active dumbbell model with a confining geometry given by the following polar curves:

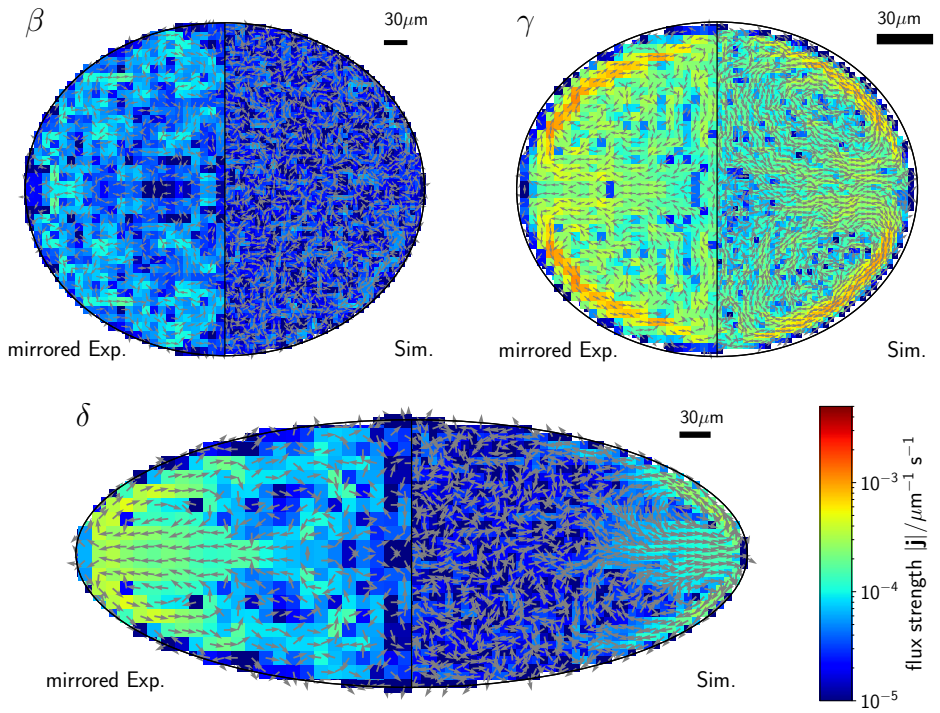

FIG. S5. Further comparison of probability fluxes extracted from experiments (left half of each panel) and simulations (right half of each panel). Steady-state nonequilibrium fluxes with arrows indicating their direction and their strength encoded with color. The panel labels β, γ, δ identify the shapes shown in Fig. 4 in the main text.

Shape of compartment A):

$$\frac{r(\theta)}{A} = 2 + \cos(\theta) + 0.1 \sin\left(2\theta + \frac{\pi}{3}\right) \tag{S28}$$

Shape of compartment B):

$$\frac{r(\theta)}{A} = 1 + \sin^2(2\theta) + \frac{1}{2}\sin^2\left(\frac{3}{2}\left[\theta - \frac{\pi}{2}\right]\right) + \frac{1}{2}\sin^2\left(\frac{1}{2}\left[\theta - \frac{\pi}{4}\right]\right) \tag{S29}$$

Shape of compartment D):

$$\frac{r(\theta)}{A} = 1 + \cos^2(1.5\theta) + 0.1 \sin\left(2\theta + \frac{\pi}{3}\right) \tag{S30}$$

Shape of compartment E):

$$\frac{r(\theta)}{A} = 1 + \cos^2(\theta) + 0.1 \sin^2\left(1.5\theta + \frac{\pi}{3}\right) \tag{S31}$$

Shape of compartment G):

$$\frac{r(\theta)}{A} = \frac{9 + \cos(6\theta)}{10} \tag{S32}$$

Shape of compartment H):

$$\frac{r(\theta)}{A} = \cos^3(\theta) + \sin^5(\theta) \tag{S33}$$

where $A = 80\,\mu\text{m}$ is the same for all compartments in Eq. (S28)-(S33).
Compartments C) and F) are superellipses given by the polar curve:

$$r(\theta) = \frac{AB}{\left(|B\cos(\theta)|^4 + |A\sin(\theta)|^4\right)^{1/4}} \tag{S34}$$

with $A = B = 80\,\mu\text{m}$ for compartment c) and $A = 150\,\mu\text{m}$, $B = 80\,\mu\text{m}$ for compartment f).

We also show additional comparisons between experiments and simulations in Fig. S5. The panel labels β, γ, δ correspond to the calculations shown in Fig. 4 in the main text. Each panel shows the experimentally obtained probability fluxes (left half of each panel), and the probability fluxes obtained from our simulations of the dumbbell model for *Chlamydomonas* (right half of each panel).

VII. SUPPLEMENTARY VIDEO LEGEND

SI Video: Video of a single *Chlamydomonas reinhardtii* cell (strain SAG 11-32b) swimming within a stand-alone elliptical microfluidic compartment with a major semi-axis of 157 µm and a minor semi-axis of 63 µm.

[1] C. Battle, C. P. Broedersz, N. Fakhri, V. F. Geyer, J. Howard, C. F. Schmidt, and F. C. MacKintosh, Broken detailed balance at mesoscopic scales in active biological systems, Science **352**, 604 (2016).

[2] T. Ostapenko, F. J. Schwarzendahl, T. J. Böddeker, C. T. Kreis, J. Cammann, M. G. Mazza, and O. Bäumchen, Curvature-guided motility of microalgae in geometric confinement, Phys. Rev. Lett. **120**, 068002 (2018).

[3] A. Liemert and A. Kienle, Exact solution of poisson's equation with an elliptical boundary, Applied Mathematics and Computation **238**, 123 (2014).